Mechanistic Insights into the Ceria-Catalyzed Synthesis of Carbamates as Polyurethane Precursors

Begoña Puértolas,[†,⊥] Marcos Rellán-Piñeiro,[‡,⊥] José Luis Núñez-Rico,[‡,⊥] Amol P. Amrute,[†] Anton Vidal-Ferran,*[‡,§] Núria López,*[‡] Javier Pérez-Ramírez,*[†] and Stefan Wershofen[∥]

[†]Institute for Chemical and Bioengineering, Department of Chemistry and Applied Biosciences, ETH Zurich, Vladimir-Prelog-Weg 1, 8093 Zurich, Switzerland

[‡]Institute of Chemical Research of Catalonia and The Barcelona Institute of Science and Technology, Avinguda dels Països Catalans 16, 43007 Tarragona, Spain

[§]Institució Catalana de Recerca i Estudis Avançats, Passeig de Lluís Companys 23, 08010 Barcelona, Spain

[∥]Covestro Deutschland AG, Kaiser-Wilhelm-Allee 60, 51373 Leverkusen, Germany

Ⓢ *Supporting Information*

ABSTRACT: The methoxycarbonylation of toluenediamines with dialkyl carbonates constitutes an alternative route for the phosgene-free production of isocyanate precursors. Despite the remarkable catalytic activity of ceria in the reaction, achieving full selectivity and long-term stability still represent major challenges. Here, the mechanism of the methoxycarbonylation of the industrially relevant 2,4-diaminotoluene (2,4-TDA) with dimethylcarbonate (DMC) along with the evolution of the property−performance interplay upon consecutive cycles are rationalized via the identification of reaction products, characterization tools, and density functional theory (DFT). The formation of the desired carbamates (7% mono- and 83% biscarbamate) is favored over the (111) facet, the most abundant in the as-prepared material, and proceeds via a complex reaction mechanism that involves a broad number of isomers and multiple reaction paths. A consecutive reaction in which 2,4-TDA is converted into a monocarbamate that further reacts to the biscarbamate drives the selective path. Part of these carbamates reacts to form productive ureas, unprecedented intermediates that reversely transform into carbamates. A full product analysis enables us to identify a number of side products that mostly comprises N-methylated carbamates and N-methylated ureas. Evaluation in subsequent cycles evidences the catalyst deactivation and the concomitant increase in the formation of byproducts, which is linked to the increasing amount of carbon deposits along with the DMC-induced partial surface restructuring into an oxygen-defective (100) facet after six cycles. These findings highlight the challenges in the rational design of robust heterogeneous catalysts for the production of isocyanate precursors.

KEYWORDS: *carbamates, ceria, deactivation, isocyanate precursors, methoxycarbonylation mechanism, structure sensitivity, ureas*
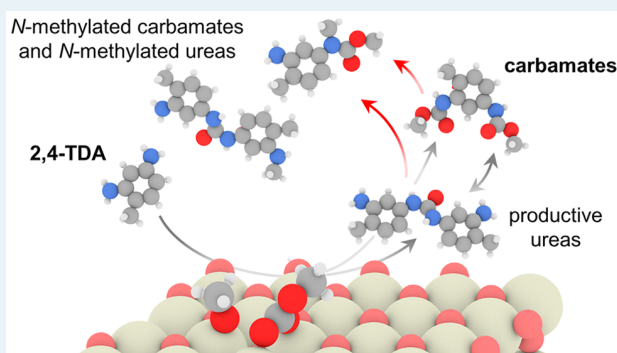
1. INTRODUCTION

Aromatic di- and polyisocyanates (e.g., toluene diisocyanates, TDI) are of great commercial relevance in the manufacture of polyurethanes.[1] Their market size was ca. USD 65.5 billion in 2018 and is projected to grow at an annual rate of 7% until 2025 driven by the increasing demand for lightweight and durable materials in the furniture, construction, electronics, and automotive industries.[2] The current manufacture of TDI relies on the use of phosgene as building block to transform both primary amino groups of 2,4-diaminotoluene (2,4-TDA) into isocyanate motifs.[3] The process is highly selective and facile, and so far, there are no alternative technologies available to produce aromatic isocyanates economically on an industrial scale. However, the high toxicity of phosgene and extraordinary safety precautions associated with its use prompt the search of greener chemical routes.[1] Carbamates, which can be readily transformed into isocyanates by thermal decomposition, have become an appealing substitute for the synthesis of polyurethanes. They can be produced by the catalytic alkoxycarbonylation of diamines with dialkyl carbonates, such as dimethylcarbonate (DMC), with the corresponding formation of an alcohol as the only byproduct, which is easily recyclable to yield the dialkyl carbonate in a second stage. Zinc acetate and zinc aggregates have been reported as efficient catalysts (ca. 99% yield of biscarbamates),[4,5] but their limited reusability prevents their implementation at technical scale.

Scheme 1. Simplified Reaction Network of the N-Methoxycarbonylation of 2,4-TDA with DMC over CeO$_2$[a]
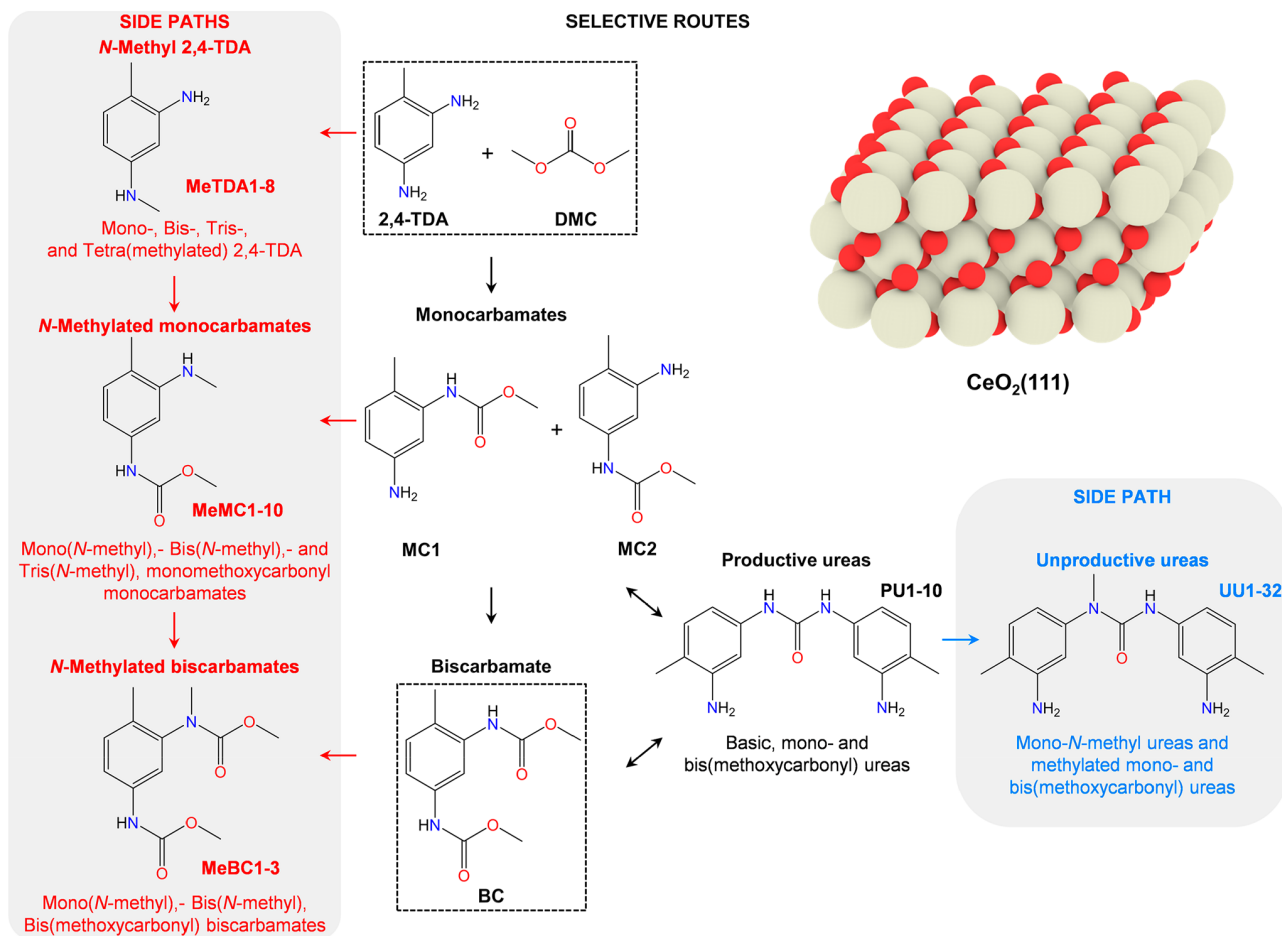
[a]The detailed list of structures is provided in Section S2 of the Supporting Information.

To overcome these limitations, the quest of efficient heterogeneous catalysts has been pursued.[6−13] Several metal oxides such as CeO$_2$, ZrO$_2$, ZnO, or TiO$_2$, supported metal oxides over aluminophosphates, mesoporous silicas, or activated carbons, heterogenization of the homogeneous zinc acetate moiety, and metal−organic framework (MOF)-based systems have been explored. Among them, nanocrystalline ceria emerged as a unique catalyst for the methoxycarbonylation of 2,4-TDA (Scheme 1). Assessment in catalysis evidenced that the exposure of (111) or (110) facets of CeO$_2$ led to ca. 90% yield of carbamates and 10% of side products, whereas the latter doubled over the (100) facet. Laursen et al. studied the reaction mechanism by first-principles without considering the van der Waals contributions and using aniline as surrogate of 2,4-TDA.[14] The formation of the desired carbamates was driven by the selective DMC dissociation to yield O$_{latt}$−COOCH$_3$ (O$_{latt}$: lattice oxygen) over the (111), (110), and (100) facets, whereas the formation of methylated products occurred over the (100) facet. Only identification of the selective reaction products was conducted. Stability studies addressing the potential impact of successive reaction cycles on the catalytic performance and on the properties of the catalyst were not reported.

In order to advance the understanding of this system, the present study analyzes the reaction mechanism of the methoxycarbonylation of the industrially relevant 2,4-TDA with DMC catalyzed by CeO$_2$. Characterization results along with full product analysis at intermediate and final stages of the reaction and atomistic modeling are applied to identify the paths leading to the desired and side products. Impact evaluation of the catalyst restructuring on the evolution of the performance with the number of cycles enables identification of the mechanistic routes resulting in the observed catalyst deactivation, which remains as the key challenge for making this technology of commercial appeal.

2. EXPERIMENTAL SECTION

2.1. Catalyst Preparation and Characterization. CeO$_2$ was prepared by precipitation following a previously reported protocol.[15] Briefly, Ce(NO$_3$)$_3$·6H$_2$O (Acros, 99.5%) was dissolved in deionized water in a weight ratio of 1:10 under stirring and H$_2$O$_2$ (Aldrich, 35%) was added to the solution to obtain a molar H$_2$O$_2$/Ce ratio of 3. The precipitation was achieved by the addition of aqueous NH$_4$OH (Aldrich, 30%) until reaching a pH of 10.5. The slurry was stirred for 4 h, and the solid was separated by filtration, washed with deionized water, dried overnight at 373 K, and calcined in static air at 773 K for 5 h using a heating rate of 5 K min^{-1}.

Powder X-ray diffraction (XRD) was measured using a PANalytical X'Pert PRO-MPD diffractometer and Cu Kα

radiation (λ = 0.15418 nm). The diffraction data was recorded in the 10−70° 2θ range with an angular step size of 0.017° and a counting time of 0.26 s per step. N_2 sorption at 77 K was measured in a Micromeritics TriStar II analyzer. Prior to the measurement, the solid was outgassed at 573 K for 3 h. The Brunauer−Emmett−Teller (BET) method was applied to calculate the total surface area, S_{BET}, in square meters per gram. Samples for high-resolution transmission electron microscopy (HRTEM) studies were prepared by dusting respective powders onto carbon-coated nickel grids. Imaging was performed on a Talos F200X instrument operated at 200 kV and equipped with a FEI SuperX detector. Temperature-programmed reduction with hydrogen (H_2-TPR) was performed in a Micromeritics Autochem II 2920 analyzer. First, the solid was loaded into a U-shaped quartz micro-reactor, pretreated in air (20 cm³ min⁻¹) at 773 K for 1 h, and cooled to 323 K. The H_2-TPR analysis was carried out in 5 vol % H_2/N_2 (20 cm³ min⁻¹), ramping the temperature from 323 to 1073 K at 10 K min⁻¹. The content of carbonaceous deposits in the used catalysts was determined by thermogravimetric analysis (TGA) using a Linseis TGA PT1600 thermobalance. The solid (ca. 25 mg) was placed in an alumina crucible and heated in 5 vol % O_2/Ar (300 cm³ STP min⁻¹) from ambient temperature to 1173 at 10 K min⁻¹. Raman spectroscopy was carried out in a confocal Raman microscope (WITec CRM 200) using a 532 nm diode laser. The microscope was operated in the backscattering mode with a 100× objective lens and 6 mW power.

2.2. Evaluation of Catalyst Performance. Methoxycar-bonylation reactions were performed in a 25 cm³ stainless steel autoclave (Berghof high-pressure reactor BR-25). In a typical experiment, the catalyst was placed in the Teflon vessel together with 2,4-TDA (396 mg, 3.2 mmol, Aldrich, 98%) and the required amount of DMC (8.2 cm³, 97.2 mmol, Aldrich, 99%). Prior to the catalytic test, DMC was dried with a 4 Å molecular sieve to ensure a final water content <30 ppm, as determined by the Karl Fischer method. The weight of catalyst added to the reaction mixture was varied in the range of 0.95−1.18 g, in order to keep a fixed ratio of 20 m² mmol⁻¹ of 2,4-TDA. The total surface area was measured prior to the test as described in the previous section. Afterward, the autoclave was closed, placed in an aluminum heating block, and purged with N_2. Stirring was then started (810 rpm), and reaction times up to 10.5 h were studied. The temperature was controlled by a thermocouple connected to the heating plate. At the end of each experiment, the autoclave was removed from the heating block and cooled down in an ice−water bath for 30 min. The autoclave was then opened, the catalyst recovered by filtration, the Teflon vessel and the solid residue were washed with acetone (five times, 5 cm³), and the combined organic fractions concentrated under vacuum to give the reaction mixture, whose composition was subsequently analyzed as detailed in the next section. The recovered catalyst was placed in an open glass vial and heated in air at 393 K for 1 h prior to its storage or further reuse. Six consecutive catalytic tests (reaction time per cycle = 7.5 h) were conducted under the same conditions as those described above. After each run, the catalyst was recovered by filtration and washed with acetone as previously detailed. In order to evaluate the impact of the solvent on the properties of the catalyst, the as-prepared CeO_2 was subjected to a 42-h treatment in DMC under the same conditions to those applied in the catalytic tests. The resulting material was filtered and washed with acetone prior to

characterization and further catalytic studies in methoxycar-bonylation reactions.

2.3. Product Analysis. An Agilent 1100 series high-performance liquid chromatography (HPLC) system was used to identify all products and to quantify components of the reaction mixture. The analytical conditions were as follows: Kromasil 100 C18 column (5 μm, 4.6 mm × 150 mm); T = 298 K; flow = 1.0 cm³ min⁻¹; injection = 5 × 10⁻³ cm³; UV detection = 225 nm; eluent A, 100 cm³ of CH_3CN, 900 cm³ of H_2O, 0.01 M NH_4COOCH_3; eluent B, 900 cm³ of CH_3CN, 100 cm³ of H_2O, 0.01 M NH_4COOCH_3; gradient, 0 min 100% A, 22 min 100% A, 48 min 80% A and 20% B, 60 min 55% A and 45% B, 80 min 55% A and 45% B, 82 min stop. Up to 24 different peaks in the chromatograms of the methoxycarbony-lation reaction mixtures were identified. Analyses in a HPLC system equipped with an atmospheric pressure chemical ionization detector in positive mode (APCI⁺) using the above-mentioned chromatographic method allowed recording the mass spectra (MS) of all chromatographic peaks. The list of compounds, retention times, and diagnostic mass-to-charge (m/z) ratios of the APCI⁺-MS spectra are summarized in Section S2. Yields of 2,4-TDA, MC1 and MC2 monocarba-mates, and biscarbamate (BC) were determined employing external standards either purchased or prepared in house and quantification methods previously published by some of us.[4] The remaining obtained byproducts are not available commercially, and thus, their concentrations are calculated based on the relative area (area %) of each component determined by HPLC analysis. The assignment of the chromatographic peaks to the corresponding products is based on the mass spectra of each compound that is collected by using an APCI⁺. Productive urea PU1 (Scheme 1) was detected in real methoxycarbonylation reaction mixtures by HPLC analyses at short reaction times, while PU2 and PU3 were not detected at an appreciable extent at any time in any reaction mixture. From all productive monomethoxycarbony-lated ureas derived from PU1−3, four isomers out of four (i.e., four peaks with molecular ions in HPLC−APCI⁺ being in agreement with the corresponding [M+H]⁺ ion) were detected in the reaction mixtures (Section S3). A minimum of two isomers out of three of productive bis(methoxycarbonylated) ureas derived from PU1−3 were identified. N-Methylated compounds derived from 2,4-TDA (MeTDA1−8) were only detected in minor amounts after four consecutive cycles with the CeO_2 catalyst and in the absence of catalyst. With respect to N-methylated monocarbamates derived from MC1 and MC2 (MeMC1−10), a minimum of five isomers were detected. The three isomers of N-methylated biscarbamates derived from BC (MeBC1−3) were identified. Finally, a minimum of five isomers of N-methylated ureas UU1−32 were detected.

2.4. Computational Details. Density functional theory (DFT) simulations were performed with the Vienna Ab Initio Simulation Package (VASP, version 5.4.4).[16,17] The Perdew−Burke−Ernzerhof (PBE) functional[18] coupled to vdW-D3[19] was employed. Projector-augmented wave (PAW) pseudopo-tentials were used to describe the inner electrons, whereas valence electronic states were expanded in plane waves with an energy cutoff of 500 eV.[20] The Hubbard correction[21] of 4.5 eV was applied to the Ce (4f) states, which was optimized through a linear response method[22] and benchmarked against hybrid methods by some of us.[23] Spin-polarized calculations were performed when required. The criteria for electronic and
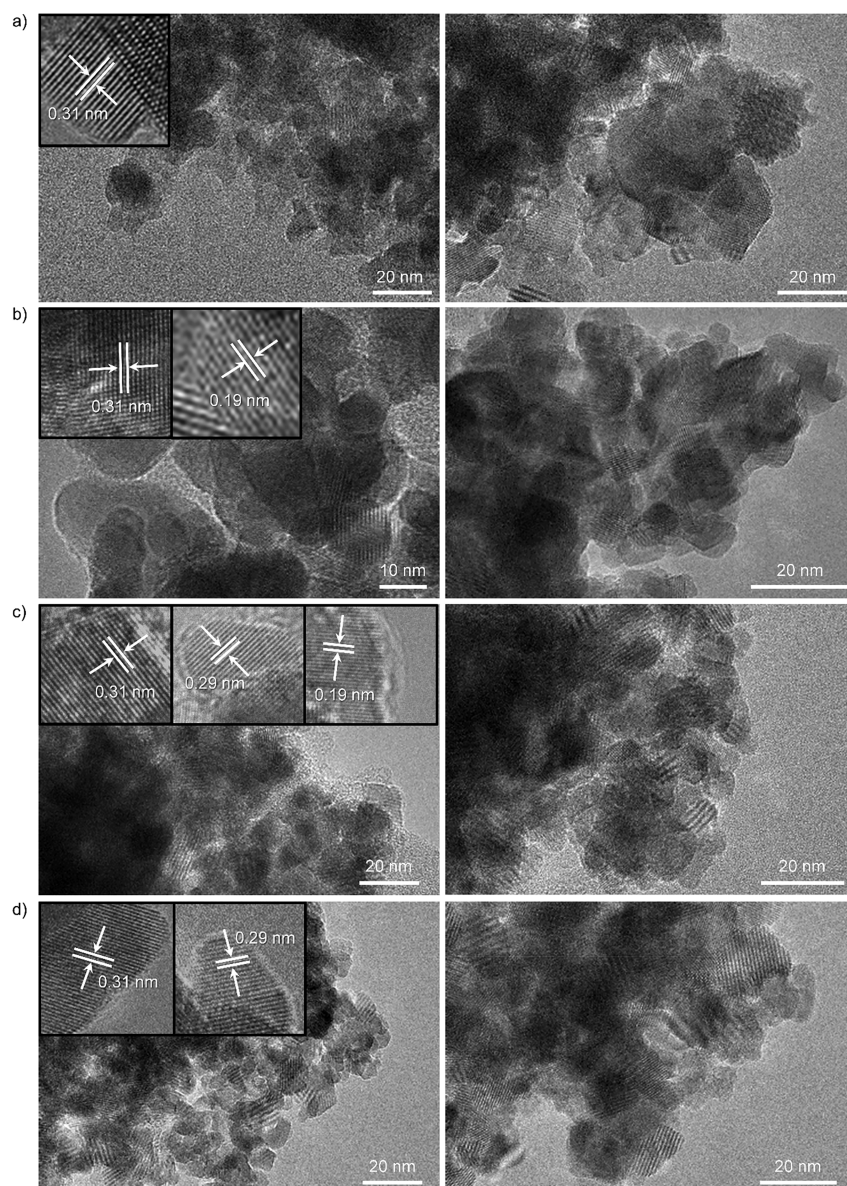
Figure 1. HRTEM of CeO$_2$ in (a) fresh form, after (b) three and (c) six consecutive cycles, and after (d) a 42-h treatment with DMC.

geometric optimization convergence were set to 10^{-6} eV and 0.025 eV Å^{-1}, respectively. The simulations were performed using the fluorite phase of CeO$_2$, as observed experimentally by X-ray analysis. The bulk was optimized with a dense $7 \times 7 \times 7$ Γ-centered k-point mesh obtaining a lattice parameter (a_{calc} = 5.470 Å) in good agreement (1.1% deviation) with the experimental value (a_{exp} = 5.411 Å).[24] The reaction mechanism was investigated on the three stoichiometric CeO$_2$ facets, i.e., (111), (110), and (100), using slab models with three, five, and four O−Ce−O trilayers, respectively. These slabs thicknesses were already tested in previous works.[25−28] For the (111) and (110) facets, there is only one surface termination that is stable. On the other hand, due to the polar character of the (100) facet, a surface reconstruction is needed and several terminations are possible. The most stable reconstruction, in which a half-monolayer of oxygen atoms is removed from the top of the slab and placed on the bottom, was considered.[29] A vacuum gap of 15 Å between slabs was added, and the dipole correction along z-axis was utilized to prevent the spurious terms arising from the asymmetry of the slabs.[30] The supercells were large enough to avoid the interaction between the adsorbates of neighboring cells and the k-points mesh was always denser than 0.3 Å^{-1}. In addition to the adsorbates, the topmost layers of the slabs, i.e., five, three, and five atom layers for the (111), (110), and (100) facets, respectively, were allowed to relax. All the molecules were computed inside a box of $20 \times 21 \times 22$ Å^3. For the reactivity in solution, the DMC solvation contributions were included through the VASP-MGCM continuous model.[31,32] The climbing image nudged elastic band (CI-NEB) method[33,34] refined with the improve dimer method (IDM)[35,36] was used to allocate the transition states. The corresponding vibrational analysis was used to characterize the intermediates and transition states in the reaction network. All the relevant structures are published in the ioChem-BD database.[37]

Table 1. Recycling Results of CeO_2 in the Methoxycarbonylation of 2,4-TDA with DMC[a,b]

cycle no.	S_{BET} (m² g⁻¹)[c]	$X_{2,4-TDA}$ (%)[d]	Y_{MC} (%)[e]	Y_{BC} (%)	Y_{MeTDA} (%)	MeC (area %)[f]	PU + UU (area %)[f]	unknown (area %)[f]	C_{bal} (%)[g]
1	64	100	7	83	0	3	4	1	98
2	55	100	9	83	0	3	2	2	99
3	58	100	26	60	0	4	2	1	93
4	62	100	23	43	<1	7	4	2	79
5	57	89	34	8	4	15	4	8	84
6[h]	68	80	12	4	11	33	2	7	89

[a]Reaction conditions: DMC/2,4-TDA = 30:1, catalyst loading = 20 m² mmol⁻¹ of 2,4-TDA, 413 K, 7.5 h, autogenous pressure. [b]Values are expressed as an average of all independent runs. The structures corresponding to each group of compounds are shown in Section S2 of the Supporting Information. [c]Surface area of the catalyst prior to each catalytic cycle. The weight of catalyst added to the reaction mixture was varied in the range of 0.95−1.18 g, in order to keep a fixed ratio of 20 m² mmol⁻¹ of 2,4-TDA. [d]Conversion of 2,4-TDA. [e]Corresponds to the sum of the yields of the para and ortho isomers. [f]Not quantified; results are expressed as area %. [g]Sum of all the detected species. $C_{bal} = (100 - X_{TDA}) + \sum Y_{MC,BC,MeTDA} + \sum$ area %$_{MeMC, MeBC, PU, UU, unknown}$. [h]The values of the sixth cycle correspond to the results after regeneration of the catalyst with DMC.

3. RESULTS AND DISCUSSION

3.1. Characterization of CeO_2 and Evaluation in the Methoxycarbonylation of 2,4-TDA.
Characterization of the as-prepared material by XRD (Figure S1a) revealed the characteristic pattern of the cubic fluorite structure of CeO_2, and application of the Scherrer equation to the most prominent (111) reflection led to an average crystallite size of 11 nm. The sample exhibited a total surface area of S_{BET} = 64 m² g⁻¹. The H_2-TPR results (Figure S1b) evidenced the characteristic low-temperature peak at around 600−800 K, attributed to the reduction of surface oxygen species, and a high-temperature peak >900 K, associated with the bulk reduction of CeO_2.[38] HRTEM analysis (Figure 1a) revealed the presence of octahedron-like geometry CeO_2 particles of variable diameter (ca. 10 nm) in which the dominant lattice fringes (0.31 nm) correspond to the (111) family.

The CeO_2 catalyst was evaluated in the methoxycarbonylation of 2,4-TDA with DMC (Table 1) under the standard reaction conditions, i.e., 20 m² mmol⁻¹ of 2,4-TDA, 413 K, 7.5 h. The substrate was fully converted to yield 7% of monocarbamates (mixture of the MC1 and MC2 isomers) and 83% of biscarbamate (BC). The results were reproducible, and the standard deviation values for the yields of MC1, MC2, and BC after six independent runs were 0.6% for the sum of MC1 and MC2 and 1.5% for BC. Additionally, formation of side products, i.e., 3 area % of N-methylated carbamates (MeC1−13), 1 area % of productive ureas (PU1−7), and 3 area % of N-methylated ureas (UU1−32), was observed under these conditions along with 1 area % of unidentified compounds.

The concentration profiles of 2,4-TDA, productive and unproductive intermediates, and the target compounds as a function of the reaction time are displayed in Figure 2. The evolution of the carbamates (i.e., MC1, MC2, and BC) corresponds to that typically observed in competitive sequential processes: the starting amine was first converted into monocarbamates (MC1 and MC2), which were then consumed to form the final BC product at longer reaction times (Figure 2a). Interestingly, an additional compound with a similar concentration profile to that of MC1 or MC2 was observed at short reaction times. HPLC−APCI⁺ analyses and chemical synthesis allowed us to identify the structure of this unprecedented intermediate as 1,3-bis(3-amino-4-methylphenyl)urea (structure PU1 in Section S2), for which a maximal 10 area % content at ca. 15 min was determined. While other isomers of PU1 were not detected, monomethox-

ycarbonylated (compounds PU4−7 with a maximal 7 area % content at ca. 40 min) and bis(methoxycarbonylated) (compounds PU8−10 with a maximal 6 area % content at ca. 110 min) ureas were also identified (Figure 2b). Following an analogous trend to that observed for PU1, mono- and bis(methoxycarbonylated) PU4−10 ureas were also consumed at extended reaction times, which prompted us to investigate if the final carbamates could arise from these intermediates. Therefore, PU1 was synthesized and allowed to react under the standard reaction conditions yielding a reaction mixture that was mainly composed by carbamates (Table S1), thus suggesting the key role of CeO_2 in the formation of the carbamates, as no methoxycarbonylation of the starting material or cleavage of the productive ureas into MC or BC occurred to an appreciable extent in the absence of the catalyst. These results point to a number of competitive sequential processes involving MC1, MC2, and the productive ureas (Scheme 1), which are converted to the target BC at late stages in the CeO_2-catalyzed process. The complete reactivity of ureas will be studied in detail in an upcoming work. Regarding the formation of side products (Figure 2c), the concentration of N-methylated carbamates and ureas (i.e., MeMC, MeBC, and UU derivatives) increases with time, reaching a plateau in the case of the N-methylated ureas, thus highlighting the significance of shortened reaction times.

In order to assess the reactivity of the 2,4-TDA, reaction intermediates, and the target biscarbamate product in the absence or presence of CeO_2 and/or using different reaction temperatures or times, additional reference experiments were conducted (Table S1). 2,4-TDA was subjected to methoxycarbonylation conditions in the absence of catalyst (DMC, 413 K, 7.5 h) yielding 10% MeTDA derivatives. In this case, carbamates MC1, MC2, or BC were not detected. The comparison of these results with those attained under catalytic conditions (Table 1) suggests that (i) CeO_2 is key in the formation of the selective and side products and (ii) any trace of MeTDA derivatives formed in solution can evolve into the different side products, i.e., N-methylated carbamates and ureas, detected under catalytic conditions. Indeed, MeTDA derivatives were not identified during the first cycle with CeO_2 (Table 1). Additionally, the impact of the reaction temperature on the product distribution in the methoxycarbonylation of 2,4-TDA with DMC over CeO_2 was assessed after 75 min. By contrasting the results obtained at 413 K (Figure 2, Table S1) with those at 383 K (Table S1), the accumulation of productive ureas at lower reaction temperatures was evidenced.
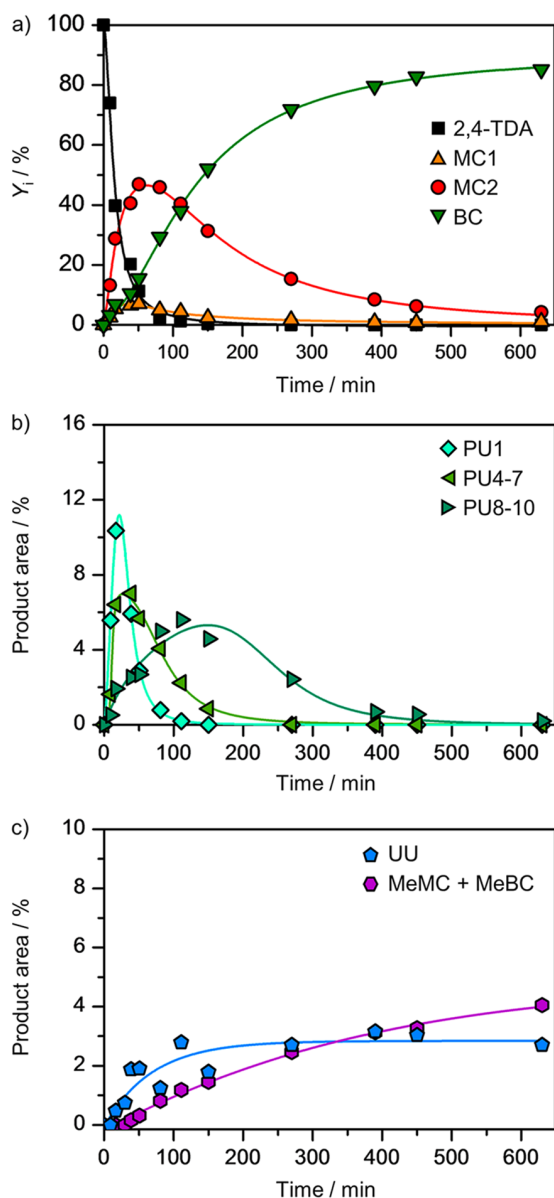
Figure 2. Concentration profiles as a function of the reaction time: (a) 2,4-TDA, MC1, MC2, and BC, (b) productive ureas (PU), and (c) N-methylated carbamates (MeMC and MeBC) and N-methylated ureas (UU). Solid lines correspond to eye guidelines. The profile corresponding to N-methylated TDA (MeTDA) is not shown as these compounds were not detected. The detailed list of structures is provided in Section S2 of the Supporting Information.

In this case, 41 area % of productive ureas was identified, from which 33 area % corresponded to PU1, whereas 10 area % [1 area % corresponds to PU1 and the rest to mono- and bis(methoxycarbonylated) ureas] was detected at 413 K. Finally, assessment of the N-methylation of the carbamate groups of BC with DMC was conducted under thermal and catalytic conditions (413 K, 7.5 h). An amount of 8% of the substrate was converted in the presence of CeO_2 leading to the formation of mono-(N-methyl) and bis(N-methyl) MeBC derivatives, whereas no N-methylated products were detected in the absence of catalyst.

3.2. Reaction Mechanism.

The mechanism for the direct synthesis of biscarbamates and side reactions in the methoxycarbonylation of 2,4-TDA with DMC was studied via DFT on CeO_2 (111) as this is the most abundant facet in the fresh material (Figure 1a). For completeness, the reaction mechanism was also derived on the other two low-energy (110) and (100) surfaces, and the main mechanistic differences are elaborated in Section S5. The complex reaction network on CeO_2 is summarized in Figure 3, and the reactivity of 2,4-TDA, carbamates, and N-methylated carbamates and ureas in solution is exemplified in Figure 4. The details of all the steps involved in the reaction network are explained in the following sections.

3.2.1. DMC Activation.

The first step in the reaction mechanism is the adsorption of DMC. It adsorbs in an $\eta_{2,C,O}$ configuration to a Ce−O_{latt} bond by −0.89 eV (Table S2). The subsequent DMC dissociation to a methoxycarbonyl group (O_{latt}−$COOCH_3$), i.e., the reactant needed for the methoxycarbonylation reaction, and a methoxy group (Ce−OCH_3) is exothermic (0.09 eV) with a small activation energy (0.20 eV). Alternatively, DMC can dissociate to form monomethyl carbonate (Ce−$OCOOCH_3$) and a surface methyl group (O_{latt}−CH_3) via an S_N2 mechanism with the O_{latt} acting as a nucleophile; both mechanisms are in line with previous studies that have tackled the dissociative adsorption of DMC on CeO_2 catalysts using in situ Fourier transform infrared (FTIR) spectroscopy.[7] The O_{latt}−CH_3 groups are potential methylating agents responsible of the formation of side products (Section S5). This dissociation is exothermic (0.33 eV) although unfeasible attending to its high activation energy (1.50 eV). As large amounts of DMC are present in the reaction mixture, the high exothermicity of the adsorption of dissociated DMC (0.98 eV) may result in the full coverage of the catalyst surface with O_{latt}−$COOCH_3$ and Ce−OCH_3 fragments. Unlike on the pristine surface, the unselective O_{latt}−CH_3 groups are easily formed if vacancies are present. DMC adsorbs stronger on an O_{latt} in contact with a Ce^{3+} center (−1.16 eV), which results in the dissociation of a methoxy group of DMC that replenishes the vacancy and leads to the formation of surface methyl groups (vide infra). This step has a small energy barrier (0.40 eV) and is highly exothermic (1.41 eV). The high energy associated with vacancy formation on this surface [2.11 eV in a (4 × 4) supercell] restricts the process to vacancies either present in the fresh catalyst or formed during the catalytic process in case surface reconstruction occurs.

3.2.2. Mechanism of the Selective Path.

Once DMC is adsorbed, the subsequent adsorption of 2,4-TDA occurs. The substrate adsorbs through one of its two amino groups on a surface cation (Figure 3) with an adsorption energy for the most accessible para group of −1.43 eV. Since the adsorption of this molecule would require the desorption of the adsorbed DMC, the replacement energy ($\Delta E_{ads,2,4-TDA} - \Delta E_{ads,DMC} = -0.45$ eV) (Table S3, Figure S7) is the one considered as a reference along the manuscript. The O_{latt} can strip a proton from the −NH_2 groups with an activation barrier of 0.56 eV (Table S4). This step is endothermic by 0.52 eV, and therefore, the equilibrium is shifted toward the reactants (Figure 5, Table S4). In the case of the ortho isomer (MC1), the steric hindrance due to the presence of the aryl-methyl group hampers both the adsorption and the −NH_2 activation, which explains the higher concentration of the MC2 isomer observed experimentally (Figure 2a). After the activation of the −NH_2 group, the subsequent formation of the monocarbamate occurs via the nucleophilic attack of the lone electron pair of
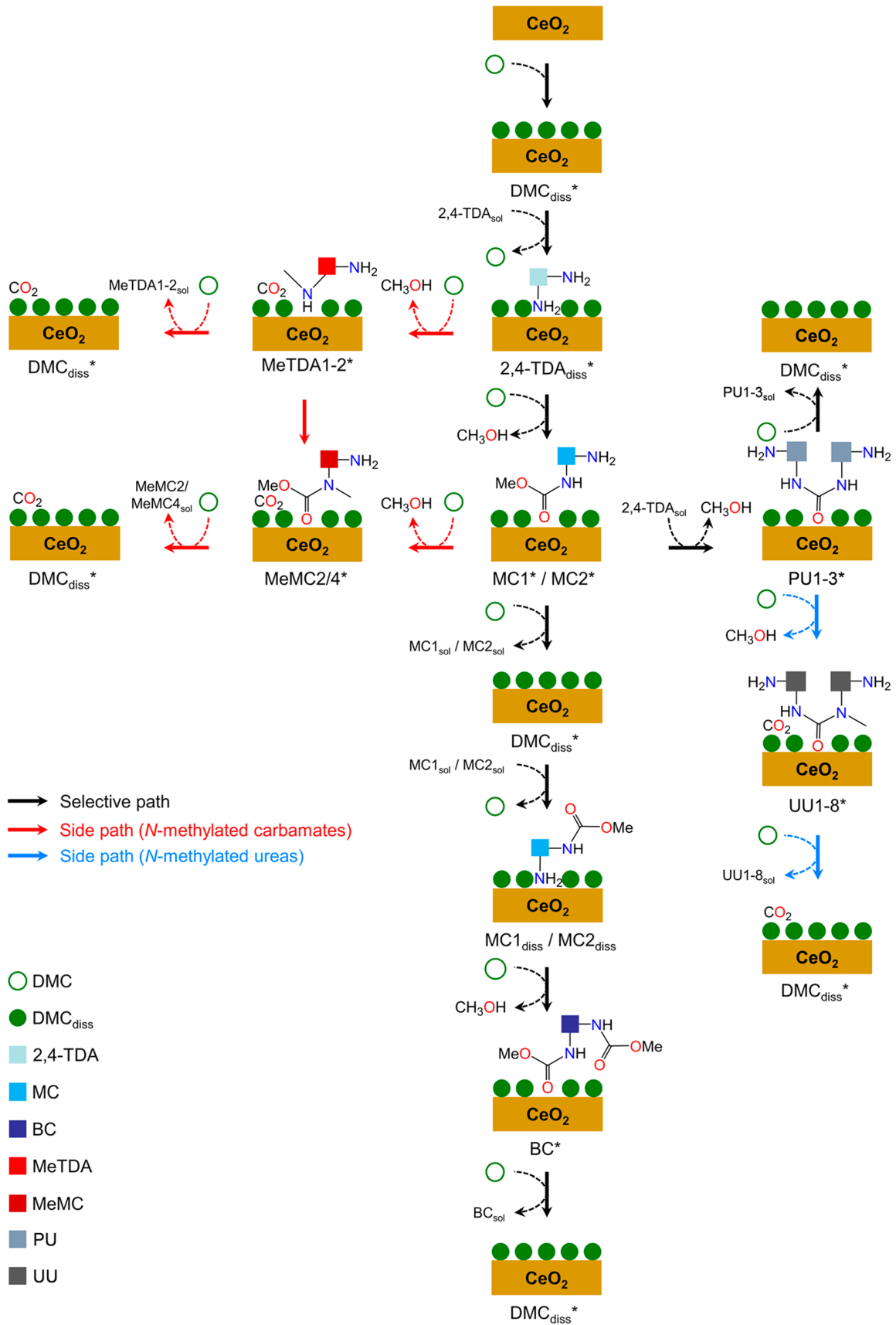
Figure 3. Reaction network of the methoxycarbonylation of 2,4-TDA with DMC on the surface of CeO_2. The selective path is shown with black arrows. The side paths leading to the N-methylated carbamates and N-methylated ureas are shown with red and blue arrows, respectively.
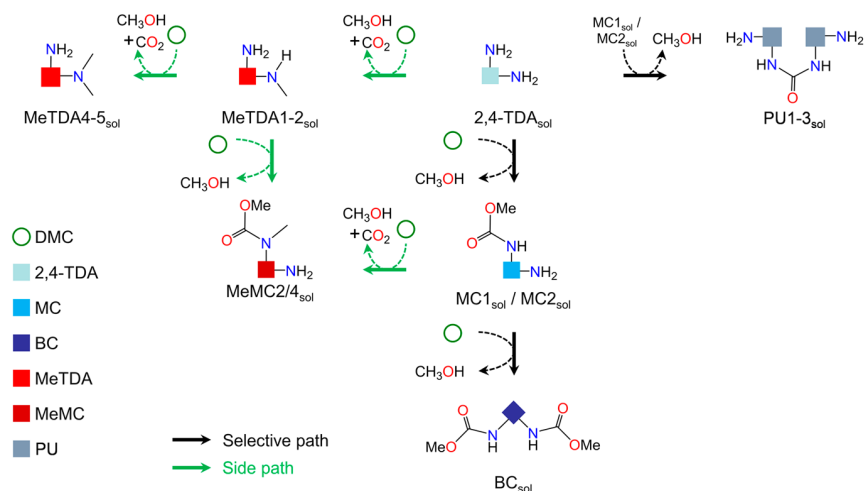
Figure 4. Reaction network of the methoxycarbonylation of 2,4-TDA with DMC in the reaction medium. The selective path is shown with black arrows. The side paths leading to the N-methylated compounds are shown with green arrows.
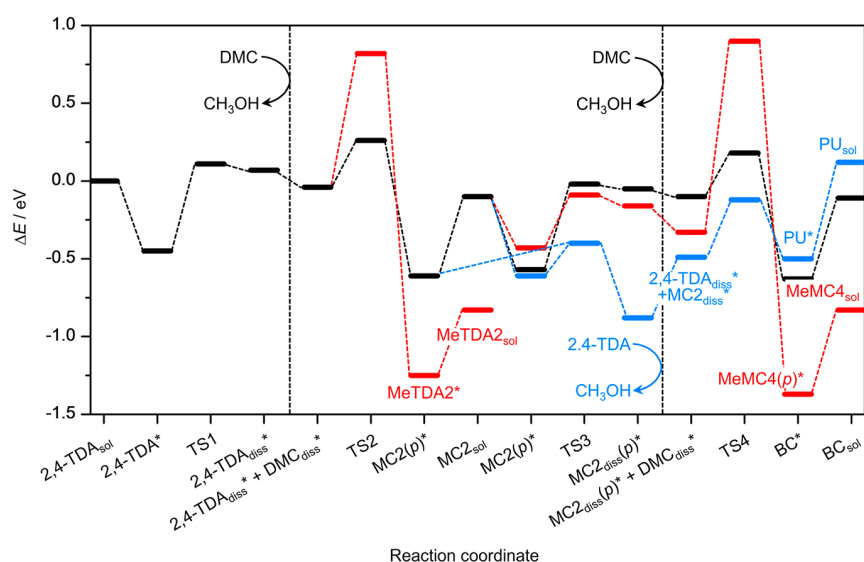

Figure 5. Reaction profiles of the selective (black) and side (red and blue for the paths leading to the N-methylated carbamates and N-methylated ureas, respectively) pathways in the methoxycarbonylation of 2,4-TDA with DMC over the stoichiometric (111) surface of CeO_2. The reaction on the most favorable para position for both the selective and side paths is considered. The asterisks denote adsorbed molecules. The position (para or ortho) of the amino group that reacts is indicated in parentheses, e.g., MC2(*p*) refers to MC2 that reacts in the para position to transform into BC.

nitrogen to the C=O group in O_{latt}-COOCH$_3$ (Figure 6).[39] The formation of MC2 is exothermic (0.42 eV) with an activation energy of 0.30 eV, and MC2 desorption energy is 0.37 eV. Similar values were obtained for the formation of MC1 via the reaction on the ortho position of 2,4-TDA (Table S4). Both MC1 and MC2 yet contain a free amino group that can dissociate on the surface and react with another methoxycarbonyl group to form the target BC product. Therefore, the desorbed MC molecules are readsorbed via their second amino group. The subsequent reaction mechanism and energy values associated to this transformation are analogous to those described above for 2,4-TDA (Table S4). The low energy requirements are in line with the full conversion of 2,4-TDA observed experimentally on the fresh material (Table 1).

3.2.3. 2,4-TDA Condensation and Formation of Productive Ureas. Ureas are formed by condensation of two aromatic ring-containing molecules that incorporate either an amino or a carbamate functional group (blue arrows in Figure 3). Productive ureas (PU4−10) constitute unprecedented intermediates in the formation of the target carbamate and a number of side products which contain the urea motif were experimentally observed (Table 1). The reaction of activated 2,4-TDA and MC2 forms the most stable productive urea, i.e., 1,3-bis(3-amino-4-methylphenyl)urea (structure PU1 in Scheme 1). The first step is the dissociation of the −OCH$_3$ moiety of the carbamate group of MC2, which can readily occur on the catalyst surface after the formation of the monocarbamate. This process is exothermic (0.28 eV) and has lower energy barrier (0.20 eV) than the competitive monocarbamate desorption (0.37 eV). Once MC2 is dissociated, the condensation product is formed by the nucleophilic attack of activated 2,4-TDA to the C=O group of the dissociated monocarbamate, which requires an
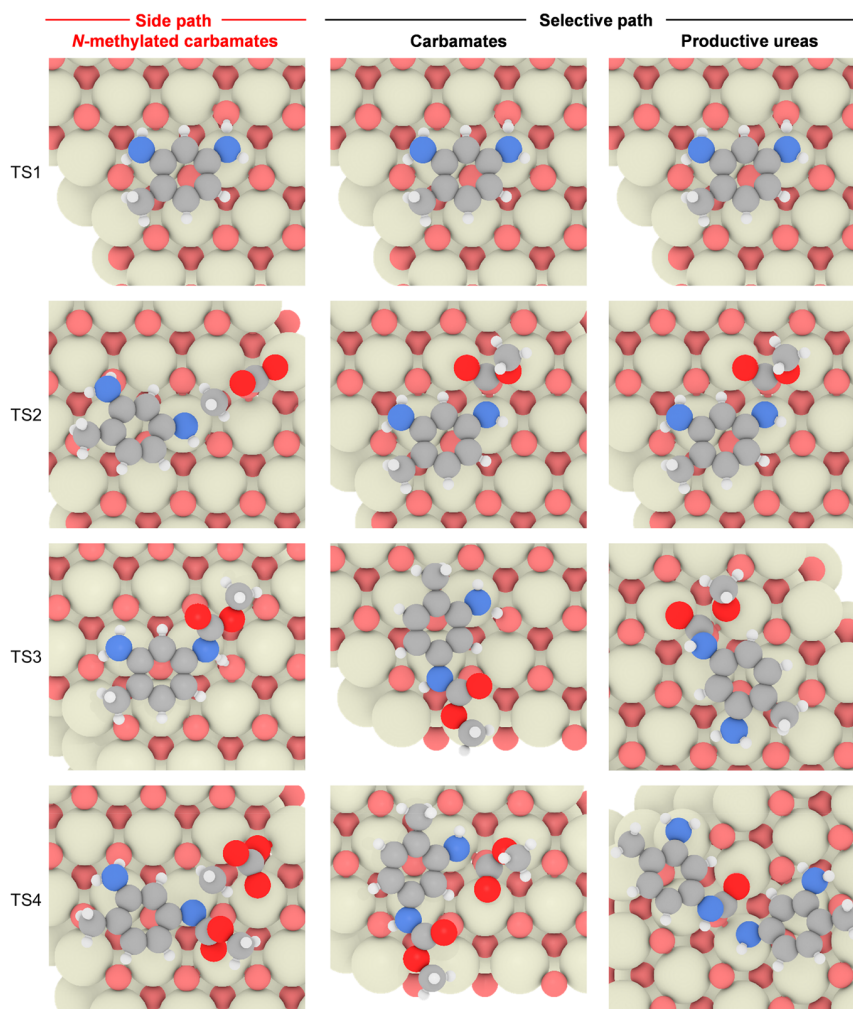
Figure 6. Top view of the DFT-optimized adsorption configuration of the transition states for the selective pathways leading to carbamates (middle) and productive ureas (right) and side pathways leading to the formation of N-methylated carbamates (left) in the methoxycarbonylation of 2,4-TDA with DMC over the stoichiometric (111) surface of CeO_2. All the structures can be retrieved from the ioChem-BD database available at ref 37.

activation energy of 0.36 eV, thus similar to the values obtained for the methoxycarbonylation reactions. The desorption energy of the resulting PU1 urea is 0.62 eV. The analogous condensation between monocarbamates and/or biscarbamates forms the rest of the observed productive ureas (PU4−10). These compounds (PU1−10) can decompose through the reverse path either into 2,4-TDA or MC, which can evolve to the carbamates as discussed previously. The condensation path resembles other routes proposed for the conversion of anilines.[40] The computed low energy barriers favor the rapid formation of these productive ureas at short reaction times in line with the experimental evidence (Figure 2b). Nevertheless, the formation of ureas is an endothermic process (e.g., 0.21 eV for the formation of PU1 urea from 2,4-TDA and MC2), and therefore, as the reaction path is reversible, they are not detected at longer reaction times (Table 1, Figure 2c). Indeed, when the reaction is conducted at lower temperatures and short reaction times (383 K, 75 min), a larger fraction of productive ureas is detected (Table S1), consistent with the lower energy demands for this transformation derived from the DFT simulations.

3.2.4. Mechanism of the Side Paths.

N-Methylated 2,4-TDA (MeTDA) derivatives, carbamates (MeMC1−10 and MeBC1−3), and ureas (UU1−32) constitute the main fraction of side products (Table 1). MeTDA, MeMC1−10, and MeBC1−3 are formed via an S_N2 reaction between either the activated amine or the carbamate groups with the methyl group of O_{latt}−$COOCH_3$ (red arrows in Figure 3).[39] On 2,4-TDA, this reaction results in the formation of N-methylated 2,4-TDA (MeTDA1 and MeTDA2) and CO_2 (Figure 3). It is highly exothermic on the most reactive para amine group (1.20 eV) and has an activation energy of 0.86 eV, which is higher than that computed for the selective path (methoxycarbonylation of 2,4-TDA, 0.30 eV) due to the different electrophilic character of the two methoxycarbonyl moieties.[39] Once MeTDA2 desorbs (0.43 eV), it is further methoxycarbonylated either on its NH_2 or $NHCH_3$ groups to form the experimentally detected N-methylated carbamates (MeMC1, MeMC4, MeMC5, MeMC6, MeMC7, MeMC9, and/or MeMC10 in Scheme 1 and Section S2), which explains that MeTDA is not detected experimentally in the catalytic reaction (Table 1). The methoxycarbonylation of the free amino group (−NH_2) of MeTDA2 proceeds similarly to the above-

explained reaction for 2,4-TDA and leads to MeMC1. However, the methoxycarbonylation of the −NHCH$_3$ group in MeTDA2 shows small energy differences with respect to the activation and methoxycarbonylation of 2,4-TDA: the activation energy for N−H dissociation is slightly higher (0.64 eV), whereas it is lower in the case of the methoxycarbonylation (0.21 eV). The desorption energy of the resulting MeMC4 is 0.33 eV. MeTDA2 could be further methylated in the same nitrogen position toward the bismethylated compound MeTDA5. This second methylation is also exothermic (1.30 eV) with an activation energy of 0.80 eV, slightly lower than the energy needed for the first methylation, and the desorption energy of the bismethylated compound is 0.43 eV. Alternatively, N-methylated carbamates can also be formed via the methylation on the carbamate group of MC1 or MC2. Herein, we have only considered the N-methylation in the carbamate group in MC2, which proceeds via the same reaction mechanism as described above: a proton of the adsorbed carbamate group is stripped via an endothermic step (0.27 eV) with a lower activation energy (0.34 eV) than that required for the dissociation of NH$_2$ groups. The methylation reaction to form MeMC4 is highly exothermic (0.88 eV) and has an activation energy of 1.05 eV, which is higher than that for the reaction with the amino group. The desorption of the formed MeMC4 requires 0.54 eV (Table S4). These methylated compounds can react with another aromatic unit following an analogous mechanism to the one described above to form the unproductive ureas (UU1−32) experimentally detected.

3.2.5. Reactivity in Solution. During the catalytic process, the primary and N-methylated amino groups and carbamates can also react with DMC in the reaction medium, i.e., without interacting with the catalyst surface, via methoxycarbonylation and N-methylation reactions (black and green arrows in Figure 4, respectively). The transition states for these reactions were allocated on the para position of 2,4-TDA, MC2 (carbamate), and MeTDA2 (N-methylated amine). The activation energies for methoxycarbonylation are 1.34, 1.93, and 1.30 eV, respectively, following the trend of the nitrogen nucleophilicity of the reactive group, which hinders the occurrence of these reactions in the solution. These reactions result in the formation of the methoxycarbonylated compound and a methanol molecule. The activation energies for N-methylation processes follow the same trend but exhibit smaller values: 0.77, 1.27, and 0.76 eV on 2,4-TDA, MC2, and MeTDA2, respectively. Monomethyl carbamate, which quickly decomposes in methanol and CO$_2$, is concomitantly formed in these reactions. Thus, the activation energies for the methoxycarbonylation are higher than for the methylation on the three groups, contrasting the behavior observed for the catalytic process.

3.3. Assessment of Catalyst Recyclability. Up to now, the performance assessment of CeO$_2$ has been limited to a single catalytic cycle. Therefore, the stability of CeO$_2$ and the possible impact of the formation of undesired compounds on the performance upon consecutive cycles were evaluated. After each run, the total surface area of the recovered catalyst was determined and the amount of catalyst was adjusted to 20 m^2 mmol^{-1} of 2,4-TDA. Even though the surface area of the catalyst remained fairly constant upon consecutive use (Table 1) and its performance remained unaffected during the first three cycles, the yield toward the desired products halved during the fourth cycle (Figure 7a), i.e., the combined yield of
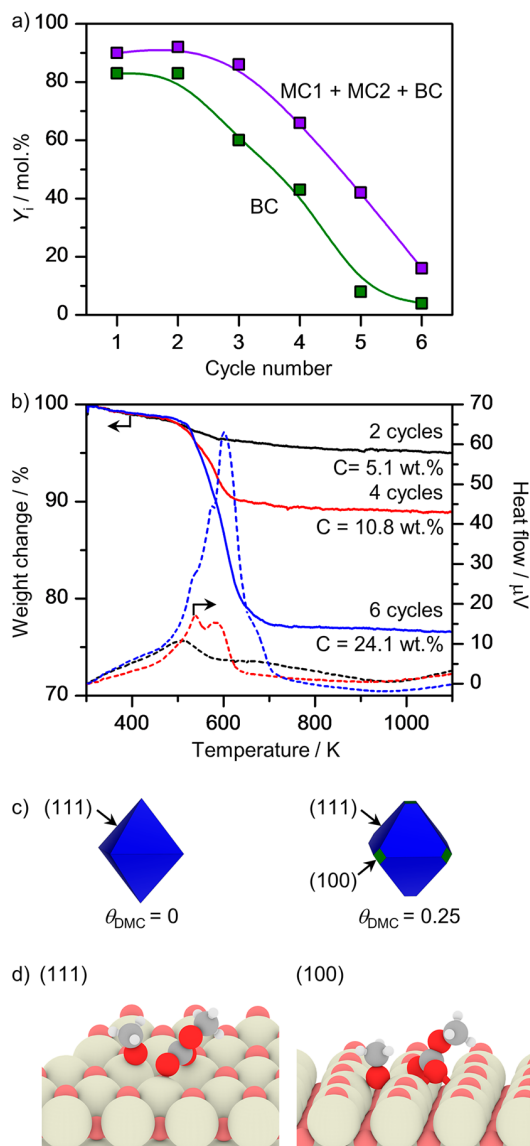

Figure 7. (a) Evolution of the yield of BC and combined yields of MC1, MC2, and BC over CeO$_2$ upon consecutive cycles. (b) Thermogravimetric analysis (TGA) in air atmosphere of CeO$_2$ after being used in the methoxycarbonylation of 2,4-TDA with DMC in different cycles. The values of the sixth cycle correspond to the results after regeneration of the catalyst with DMC. (c) Wulff constructions of dissociated DMC over stoichiometric (111) and (110) facets (blue and green, respectively) for naked, θ_{DMC} = 0, and partially DMC covered, θ_{DMC} = 0.25, CeO$_2$ nanoparticle. (d) Side view of the DFT-optimized adsorption configuration of dissociated DMC over stoichiometric (111) and (100) surfaces.

MC1, MC2, and BC decreased from ca. 90% to 40%, and further decreased during the fifth cycle. After that, the used catalyst was treated with DMC under reaction conditions (413 K, 7.5 h) in an attempt to restore the catalytic activity of the fresh material. However, the resulting material evidenced further deactivation during the sixth cycle. The decrease in the yield to the desired products was accompanied by a decrease of the 2,4-TDA conversion and an increase in the formation of undesired N-methylated carbamates (MeMC and MeBC) and ureas (UU) (Table 1) and other unknown compounds. For instance, in the case of the N-methylated carbamates, they

increased from 3 area % to 33 area % after the first and sixth cycle, respectively. XRD results of the used material (Figure S1a) revealed that the fluorite structure and crystallite size are preserved after catalysis. Characterization by TGA showed an increase in the amount of carbon deposits upon recycling, from 5.1 wt % after two cycles to 24.1 wt % after six cycles (Figure 7b), in line with the increase of the heat released via the combustion of the carbonaceous residuals. Additionally, the maximum of the heat flow profile shifted toward higher temperatures when increasing the number of cycles, suggesting the presence of heavier carbonaceous species on the catalyst surface, which might explain the decrease of the 2,4-TDA conversion after several cycles, since lower amount of active sites are available for the reaction. HRTEM micrographs of the CeO_2 samples after three and six consecutive cycles evidenced that the morphology of the CeO_2 particles is retained. Nevertheless, the occurrence of (110) facets after three cycles accompanied by the appearance of the intrinsically defective (100) facets after six cycles (Figure 1) demonstrated the surface restructuring, which led to the decrease in the selectivity to the carbamates and the concomitant increase of the formation of side products. These results are in line with previous studies,[14] in which the assessment of CeO_2 nanocubes, which preferentially exhibit the (100) facet, in this reaction led to selectivity values to the desired BC lower than 40% after 10 h, thus confirming the presence of oxygen vacancies as detrimental for the selectivity. The presence of oxygen vacancies was further corroborated by Raman spectroscopy (Figure S1c). The spectrum of the catalyst after six cycles evidenced a frequency downshift of the T_{2g} band of ca. 3 cm^{-1}, which has been previously associated to the presence of oxygen vacancies.[41]

As the catalyst is expected to be fully covered by DMC, the possible impact of the solvent on the deactivation was assessed by subjecting the CeO_2 catalyst to a 42-h treatment, i.e., the time equivalent to six consecutive cycles, with DMC. This treatment led to the occurrence of the (100) facet, as evidenced on the HRTEM micrographs (Figure 1d), which suggests the potential role of the solvent in promoting the observed surface reconstruction. The presence of DMC stabilizes the different facets in an extent proportional to its adsorption energy (per surface area), which was found very different in the three facets by DFT. This stabilization acts as thermodynamic factor of shape control that modifies the surface energies changing the surface morphology.[42,43] The surface energies of the most stable CeO_2 facets, i.e., (111), (110), and (100), result in the (111) as the only facet exposed on the fresh catalyst, as shown by the Wulff construction (Figure 7c). The (111) surface prior to the adsorption of DMC is much more stable (0.95 J m^{-2}) than the (100) surface (1.77 J m^{-2}) (Table S5). At medium coverage, i.e., $\theta_{DMC} = 0.25$, the adsorption energies per DMC molecule are very similar to those obtained on clean surfaces (−1.03 and −3.04 eV per molecule of DMC on (111) and (100), respectively) which results in stronger adsorption energies per surface area on the (100) surface [−0.020 and −0.051 eV Å^{-2} on (111) and (100), respectively]. These different adsorption energies per surface area reduce the surface energy in a different extent and result in closer surface energies of 0.64 and 0.94 J m^{-2} for (111) and (100), respectively, driving the appearance of the (100) surface as is shown in the Wulff construction in Figure 7c. The presence of intrinsic oxygen vacancies on the (100) facet favors the formation of surface methoxy groups from the selective dissociation of DMC that are equivalent to O_{latt}−CH_3 (Figure 7d). The latter are methylation agents that might lead to the increased formation of side products upon recycling (Section S5). Catalytic assessment of this material revealed lower activity than the nontreated counterpart, as yields of 16% and 72% were obtained for the desired MC and BC products, respectively, although the selectivity toward methoxycarbonylation products was not significantly affected and remained similar to that of the as-prepared material. Comparison to the results obtained after six cycles (Table 1) indicates that the absence of carbonaceous deposits in this case might also contribute to the observed differences in catalysis.

4. CONCLUSIONS

The reaction and deactivation mechanisms of CeO_2 catalysts in the methoxycarbonylation of 2,4-TDA with DMC for the production of isocyanate precursors has been assessed by a combination of experimental and theoretical tools. The as-prepared CeO_2 material exhibited 90% selectivity toward the desired carbamates, i.e., 7% p- and o-monocarbamates and 83% biscarbamate and the production of small amounts of side products. Detailed analyses of the methoxycarbonylation reaction by HPLC−APCI$^+$ at short reaction times reveal the prominent role of productive ureas in the formation of the desired carbamates via the condensation of monocarbamates and 2,4-TDA. Both paths are identified at the molecular level, and the derived energetic and kinetic parameters demonstrate the reversibility of the urea formation. N-Methylated products constitute the major fraction of the side products. Reusability tests indicate that the conversion of the substrate decreased from 100% to 80% and the selectivity to carbamates dropped to 16%, which was related to the increased formation of carbon deposits along with the surface restructuring after six consecutive cycles; whereas the fresh material mainly exhibited the (111) facet, subsequent cycles evidence the occurrence of the oxygen-defective (100) facet. The dissociation of the DMC solvent over an oxygen vacancy leads to methyl groups on the catalyst surface that favor the formation of N-methylated products. Our study not only identifies key intermediates of the reaction and deactivation mechanisms but also sets the fundamental basis behind the limited recyclability of CeO_2 providing guidelines for the design of improved catalysts for the phosgene-free production of isocyanate precursors. Upcoming studies should be directed toward the stabilization of the active exposed facet, e.g., by doping strategies, or discovering alternative active phases.

■ ASSOCIATED CONTENT

⑤ Supporting Information

Additional catalytic and characterization data, detailed list of the identified molecules, preparation and characterization of productive ureas, and DFT results (PDF)

■ AUTHOR INFORMATION

Corresponding Authors

*E-mail: avidal@iciq.cat.
*E-mail: nlopez@iciq.es.
*E-mail: jpr@chem.ethz.ch.

ORCID ●

Marcos Rellán-Piñeiro: 0000-0002-7905-9077
Amol P. Amrute: 0000-0002-3362-0842
Anton Vidal-Ferran: 0000-0001-7926-1876
Núria López: 0000-0001-9150-5941
Javier Pérez-Ramírez: 0000-0002-5805-7355

Author Contributions

[⊥]B.P., M.R.-P., and J.L.N.-R. contributed equally to this work.

Notes

The authors declare no competing financial interest.

■ REFERENCES

(1) Kreye, O.; Mutlu, H.; Meier, M. A. R. Sustainable Routes to Polyurethane Precursors. *Green Chem.* **2013**, *15*, 1431−1455.

(2) Grand View Research. Global Polyurethane (PU) Market Size & Share, 2025, Industry Report. https://www.grandviewresearch.com/industry-analysis/polyurethane-pu-market (accessed May 19, 2019).

(3) Pérez-Ramírez, J.; Mondelli, C.; Schmidt, T.; Schluter, O. F. K.; Wolf, A.; Mleczko, L.; Dreier, T. Sustainable Chlorine Recycling *via* Catalysed HCl Oxidation: from Fundamentals to Implementation. *Energy Environ. Sci.* **2011**, *4*, 4786−4799.

(4) Reixach, E.; Bonet, N.; Rius-Ruiz, F. X.; Wershofen, S.; Vidal-Ferran, A. Zinc Acetates as Efficient Catalysts for the Synthesis of Bis-isocyanate Precursors. *Ind. Eng. Chem. Res.* **2010**, *49*, 6362−6366.

(5) Reixach, E.; Haak, R. M.; Wershofen, S.; Vidal-Ferran, A. Alkoxycarbonylation of Industrially Relevant Anilines Using Zn_4O-$(O_2CCH_3)_6$ as Catalyst. *Ind. Eng. Chem. Res.* **2012**, *51*, 16165−16170.

(6) Li, F.; Li, W.; Li, J.; Xue, W.; Wang, Y.; Zhao, X. Investigation of Supported $Zn(OAc)_2$ Catalyst and its Stability in *N*-Phenyl Carbamate Synthesis. *Appl. Catal., A* **2014**, *475*, 355−362.

(7) Juárez, R.; Concepción, P.; Corma, A.; Fornés, V.; García, H. Gold-Catalyzed Phosgene-Free Synthesis of Polyurethane Precursors. *Angew. Chem.* **2010**, *122*, 1308−1312.

(8) Sun, D.-L.; Deng, J.-R.; Chao, Z.-S. Catalysis over Zinc-Incorporated Berlinite ($ZnAlPO_4$) of the Methoxycarbonylation of 1,6-Hexanediamine with Dimethyl Carbonate to Form Dimethylhexane-1,6-Dicarbamate. *Chem. Cent. J.* **2007**, *1*, 27.

(9) Guo, X.; Qin, Z.; Fan, W.; Wang, G.; Zhao, R.; Peng, S.; Wang, J. Zinc Carboxylate Functionalized Mesoporous SBA-15 Catalyst for Selective Synthesis of Methyl-4,4′-di(phenylcarbamate). *Catal. Lett.* **2009**, *128*, 405−412.

(10) Wang, Y.; Liu, B. Efficient and Recyclable Heterogeneous Zinc Alkyl Carboxylate Catalyst for the Synthesis of *N*-Phenyl Carbamate from Aniline and Dimethylcarbonate. *Catal. Sci. Technol.* **2015**, *5*, 109−113.

(11) Lucas, N.; Amrute, A. P.; Palraj, K.; Shanbhag, G. V.; Vinu, A.; Halligudi, S. B. Non-Phosgene Route for the Synthesis of Methyl Phenyl Carbamate using Ordered AlSBA-15 Catalyst. *J. Mol. Catal. A: Chem.* **2008**, *295*, 29−33.

(12) Grego, S.; Aricò, F.; Tundo, P. Phosgene-free Carbamoylation of Aniline *via* Dimethyl Carbonate. *Pure Appl. Chem.* **2011**, *84*, 695−705.

(13) Rojas-Buzo, S.; Garcia-Garcia, P.; Corma, A. Zr-MOF-808@MCM-41 catalyzed phsogene-free synthesis of polyurethane precursors. *Catal. Sci. Technol.* **2019**, *9*, 146−156.

(14) Laursen, S.; Combita, D.; Hungría, A. B.; Boronat, M.; Corma, A. First-Principles Design of Highly Active and Selective Catalysts for Phosgene-Free Synthesis of Aromatic Polyurethanes. *Angew. Chem., Int. Ed.* **2012**, *51*, 4190−4193.

(15) Moser, M.; Vilé, G.; Colussi, S.; Krumeich, F.; Teschner, D.; Szentmiklósi, L.; Trovarelli, A.; Pérez-Ramírez, J. Structure and Reactivity of Ceria-Zirconia Catalysts for Bromine and Chlorine Production *via* the Oxidation of Hydrogen Halides. *J. Catal.* **2015**, *331*, 128−137.

(16) Kresse, G.; Furthmueller, J. Efficient Iterative Schemes for *ab initio* Total-Energy Calculations using a Plane-Wave Basis Set. *Phys. Rev. B: Condens. Matter Mater. Phys.* **1996**, *54*, 11169−11186.

(17) Kresse, G.; Furthmuller, J. Efficiency of *ab-initio* Total Energy Calculations for Metals and Semiconductors using a Plane-Wave Basis Set. *Comput. Mater. Sci.* **1996**, *6*, 15−50.

(18) Perdew, J. P.; Burke, K.; Ernzerhof, M. Generalized Gradient Approximation Made Simple. *Phys. Rev. Lett.* **1996**, *77*, 3865−3868.

(19) Grimme, S.; Antony, J.; Ehrlich, S.; Krieg, H. A Consistent and Accurate *ab initio* Parametrization of Density Functional Dispersion Correction (DFT-D) for the 94 Elements H-Pu. *J. Chem. Phys.* **2010**, *132*, 154104.

(20) Kresse, G.; Joubert, D. From Ultrasoft Pseudopotentials to the Projector Augmented-Wave Method. *Phys. Rev. B: Condens. Matter Mater. Phys.* **1999**, *59*, 1758−1775.

(21) Dudarev, S. L.; Botton, G. A.; Savrasov, S. Y.; Humphreys, C. J.; Sutton, A. P. Electron-Energy-Loss Spectra and the Structural Stability of Nickel Oxide: An LSDA+U study. *Phys. Rev. B: Condens. Matter Mater. Phys.* **1998**, *57*, 1505−1509.

(22) Fabris, S.; de Gironcoli, S.; Baroni, S.; Vicario, G.; Balducci, G. Taming Multiple Valency with Density Functionals: A Case Study of Defective Ceria. *Phys. Rev. B: Condens. Matter Mater. Phys.* **2005**, *71*, 041102.

(23) Capdevila-Cortada, M.; Łodziana, Z.; López, N. Performance of DFT+U Approaches in the Study of Catalytic Materials. *ACS Catal.* **2016**, *6*, 8370−8379.

(24) Kümmerle, E. A.; Heger, G. The Structures of C−$Ce_2O_{3+\delta}$, Ce_7O_{12}, and $Ce_{11}O_{20}$. *J. Solid State Chem.* **1999**, *147*, 485−500.

(25) Capdevila-Cortada, M.; García-Melchor, M.; López, N. Unraveling the Structure Sensitivity in Methanol Conversion on CeO_2: A DFT+U study. *J. Catal.* **2015**, *327*, 58−64.

(26) Mei, D.; Deskins, N. A.; Dupuis, M.; Ge, Q. Density Functional Theory Study of Methanol Decomposition on the $CeO_2(110)$ Surface. *J. Phys. Chem. C* **2008**, *112*, 4257−4266.

(27) Beste, A.; Overbury, S. H. Pathways for Ethanol Dehydrogenation and Dehydration Catalyzed by Ceria (111) and (100) Surfaces. *J. Phys. Chem. C* **2015**, *119*, 2447−2455.

(28) Capdevila-Cortada, M.; Vilé, G.; Teschner, D.; Pérez-Ramírez, J.; López, N. Reactivity Descriptors for Ceria in Catalysis. *Appl. Catal., B* **2016**, *197*, 299−312.

(29) Capdevila-Cortada, M.; López, N. Entropic Contributions Enhance Polarity Compensation for $CeO_2(100)$ Surfaces. *Nat. Mater.* **2017**, *16*, 328−334.

(30) Makov, G.; Payne, M. C. Periodic Boundary Conditions in *ab initio* calculations. *Phys. Rev. B: Condens. Matter Mater. Phys.* **1995**, *51*, 4014−4022.

(31) Garcia-Ratés, M.; López, N. Multigrid-Based Methodology for Implicit Solvation Models in Periodic DFT. *J. Chem. Theory Comput.* **2016**, *12*, 1331−1341.

(32) Garcia-Ratés, M.; García-Muelas, R.; López, N. Solvation Effects on Methanol Decomposition on Pd(111), Pt(111), and Ru(0001). *J. Phys. Chem. C* **2017**, *121*, 13803−13809.

(33) Henkelman, G.; Jónsson, H. Improved Tangent Estimate in the Nudged Elastic Band Method for Finding Minimum Energy Paths and Saddle Points. *J. Chem. Phys.* **2000**, *113*, 9978−9985.

(34) Henkelman, G.; Uberuaga, B. P.; Jonsson, H. A. Climbing Image Nudged Elastic Band Method for Finding Saddle Points and Minimum Energy Paths. *J. Chem. Phys.* **2000**, *113*, 9901−9904.

(35) Henkelman, G.; Jónsson, H. A. Dimer Method for Finding Saddle Points on High Dimensional Potential Surfaces using only First Derivatives. *J. Chem. Phys.* **1999**, *111*, 7010−7022.

(36) Heyden, A.; Bell, A. T.; Keil, J. Efficient Methods for Finding Transition States in Chemical Reactions: Comparison of Improved Dimer Method and Partitioned Rational Function Optimization Method. *J. Chem. Phys.* **2005**, *123*, 224101.

(37) ioChem-BD Database. http://dx.doi.org/10.19061/iochem-bd-1-118.

(38) Vilé, G.; Colussi, S.; Krumeich, F.; Trovarelli, A.; Pérez-Ramírez, J. Opposite Face Sensitivity of CeO_2 in Hydrogenation and Oxidation Catalysis. *Angew. Chem., Int. Ed.* **2014**, *53*, 12069−12072.

(39) Tundo, P.; Rossi, L.; Loris, A. Dimethyl Carbonate as an Ambident Electrophile. *J. Org. Chem.* **2005**, *70*, 2219−2224.

(40) Haber, F. Gradual Electrolytic Reduction of Nitrobenzene with Limited Cathode Potential. *Z. Elektrochem. Angew. Phys. Chem.* **1898**, *22*, 506−514.

(41) Silva, I. de C.; Sigoli, F. A.; Mazali, I. O. Reversible Oxygen Vacancy Generation on Pure CeO_2 Nanorods Evaluated by in Situ Raman Spectroscopy. *J. Phys. Chem. C* **2017**, *121*, 12928−12935.

(42) Wang, Z.; Yang, G.; Zhang, Z.; Jin, M.; Yin, Y. Selectivity on Etching: Creation of High-Energy Facets on Copper Nanocrystals for CO_2 Electrochemical Reduction. *ACS Nano* **2016**, *10*, 4559−4564.

(43) Li, Q.; Rellán-Piñeiro, M.; Almora-Barrios, N.; Garcia-Ratés, M.; Remediakis, I. N.; López, N. Shape Control in Concave Metal Nanoparticles by Etching. *Nanoscale* **2017**, *9*, 13089−13094.